WEP Warwick Evans Publishing

International Journal of Natural Resources and Environmental Studies

ISSN: 3006-2012 (Print), ISSN: 3006-0834 (Online) | Volume 3, Number 1, Year 2024
DOI: https://doi.org/10.62051/ijnres.v3n1.01
Journal homepage: https://wepub.org/index.php/IJNRES/index

Simulation Study of Sand Removal Device for Geothermal Well Recharge Water

Jiayu Zhu

College of Petroleum Engineering, Xi’an Shiyou University, Xi’an 710000, China

ABSTRACT

Geothermal well recharge water is a study to protect the environment and conserve resources, while recharge water containing sand will produce clogging, the experiment is conducted by simulating the separation efficiency with different precision and time, combining the three-stage treatment process of sand removal-coarse filtration-fine filtration based on a metal wire mesh cartridge, and applying the Reynolds turbulence model of the algebraic stress model, the control equation of the flow of the airflow (k-ε) model and Reynolds stress model are considered together. The conclusion drawn from the combined considerations is that the filter media used is a wire mesh filter media, and the wellhead sand can be completely removed by three-stage filtration.

KEYWORDS

Sand Removal Device; Recharge Fluid; Hydrocyclone; Geothermal Energy; Solid-Liquid Separation.

1. INTRODUCTION

With the gradual increase in the consumption of energy problems, most of today's heat pump systems are operated in an environmentally friendly manner, there is the development of geothermal wells. After having used water from geothermal wells, groundwater is recharged back into the ground for restoring geothermal storage capacity, maintaining fluid pressure in geothermal water storage, etc.[1]. The presence of solids such as suspended solids and silt in the recharge water can lead to clogging of the geothermal water reservoir, which requires solid-liquid separation of the recharge water for desanding purposes.

Since the late sixties, solid-liquid separation recharge technology has been carried out in the United States, Germany, France and Italy; and in New Zealand, Iceland, Japan, the Philippines has also had a large number of different degrees of different applications[2]. In Beijing, the exploration and development of geothermal wells has been carried out as early as in the 50s and 60s, and the initial experimental work of recharge was carried out in the late 90s [3]. However, so far, the blockage of recharge wells has resulted in very little recharge, especially in thermal storage recharge wells in porous sandstones, which have not been effectively managed so far.

Through the study, the three-stage treatment process of desander-coarse-effect filter-fine-effect filter can obtain better filtration effect than the two-stage treatment process, and the simulation study adopts this process flow to study the way of desander, coarse-effect filter and fine-effect filter in series, and to carry out the simulation study of recharge fluid treatment equipment for the actual working conditions [4]. In order to simplify the simulation difficulty and improve the simulation accuracy, it is proposed to adopt the method of simulation of the three devices, with the average flow rate of the desander water outlet, sand content and sand particle size as the inlet conditions of the roughness filter, with the outlet conditions of the roughness filter as the inlet conditions of the fine filter, to obtain the final sand removal rate.

2. NUMERICAL SIMULATION STUDY OF DESANDER

The object of this study is two phases of water and sand, and the granular phase can be used as a dilute phase under the condition of high liquid-sand ratio[5]. The motion behavior of the particle phase mainly depends on the liquid phase flow field distribution inside the cyclone. Therefore, the liquid phase field distribution characteristics and the sand removal rate under the actual working conditions are investigated by numerical simulation methods, and then the flow parameters and sand particle physical properties at the water outlet of the desander are obtained. The three-dimensional geometric model of the fluid domain of the cyclone with a diameter of 250 mm is drawn, and the tetrahedral mesh of the cyclone is partitioned to ensure that its mesh quality is greater than 0.34 (as shown in Fig. 1). To ensure that the calculation results are independent of the number of meshes, the 250-mm cyclone is divided into five types, i.e., 800000, 980000, 136000, 188000, and 277000; and the results (as shown in Fig. 2) are compared with their velocities at z = -0.2 m. The results are shown in Fig. 2.

Fig. 1 Mesh model of 250 mm diameter cyclone

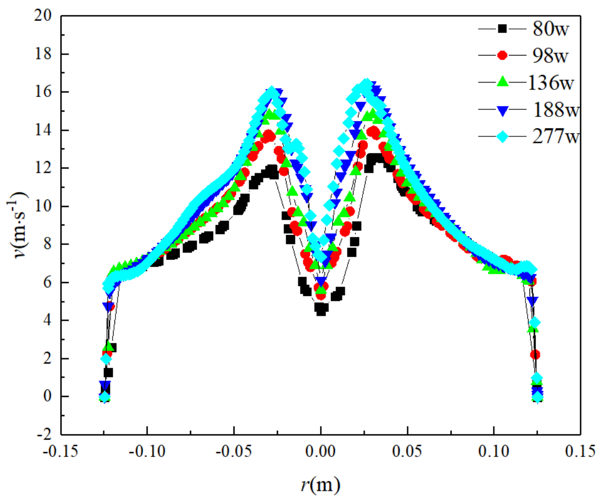

Fig. 2 Comparison of velocity at z=-0.2m with different number of grids

As can be seen from Fig. 2, with the gradual increase of the number of grids, the velocity at z=-0.2 m increases continuously from 12 m/s to 16 m/s. However, after the grid reaches 1880000 and the number of grids continues to increase, the rate of change of the velocity distribution tends to a stable state. To summarize, when the number of grids is higher than 1880000, if continue to increase the number of grids, the impact on the calculation results of this experiment is small, so the number of grids used 1880000.

3. CALCULATION CONDITIONS

Direct numerical simulation is used, which does not need to establish a turbulent flow model, but directly solves the flow control equations. Reynolds' averaging model is more widely used in engineering[6], solving Reynolds' averaging model statistically averages the mass, momentum and energy transport equations of the fluid. Reynolds turbulence models include: algebraic stress model, K-ε model and Reynolds stress model (RSM) [7]. The discrete phase model of the DPM is well suited for such cases due to the very low sand inlet content, which is essentially below 1%. The equilibrium equations for the dispersed phase particles in the flow field in Cartesian coordinate system can be given by equation[8]:

$$\frac{du_{\mathrm{p}}}{dt} = F_{\mathrm{D}}\left(u - u_{\mathrm{p}}\right) + \frac{g_{\mathrm{x}}\left(\rho_{\mathrm{p}} - \rho\right)}{\rho_{\mathrm{p}}} + F_{\mathrm{x}} \tag{1}$$

Where $F_{\mathrm{D}}\left(u - u_{\mathrm{p}}\right)$ in the trailing force per unit mass of the dispersed phase particles, and where F_{D} can be expressed as:

$$F_{\mathrm{D}} = \frac{18\mu}{\rho_{\mathrm{p}} dp^2} \frac{c_{\mathrm{D}} \mathrm{Re}}{24} \tag{2}$$

Where u and u_{p} denote the velocity of the continuous phase fluid and dispersed phase particles respectively, the dynamic viscosity of the continuous phase fluid is represented by μ, ρ and ρ_{p} denote the density magnitude of the continuous phase fluid and dispersed phase particles respectively, dp denotes the diameter of the dispersed phase particles, and Re denotes the relative Reynolds number, which can be defined by equation as follows:

$$\mathrm{Re} \equiv \frac{\rho dp \left|u_{\mathrm{p}} - u\right|}{\mu} \tag{3}$$

In the equilibrium equations for particles, other types of forces are represented F_x , the most important of which is called the “additional mass force”. This additional force results in an acceleration of the velocity of the liquid surrounding the particles in the dispersed phase which can be expressed in equation:

$$F_x = \frac{1}{2} \frac{\rho}{\rho_{\mathrm{p}}} \frac{d}{dt}\left(u - u_{\mathrm{p}}\right) \tag{4}$$

When ρ > ρ_{p} 1, the potential mass force cannot be ignored. In the flow field, an important factor that triggers the additional force is the fluid pressure gradient, which can be expressed in equation as:

$$F_x = \left(\frac{\rho}{\rho_{\mathrm{p}}}\right) u_{\mathrm{p}} \frac{\partial u}{\partial x} \tag{5}$$

Oil droplets are affected by many forces in the cyclonic flow field, but these forces act on the droplets to different degrees. In this paper, the maximum volume fraction of sand particles is set to be 1%, and under the high speed rotation, the main flow pattern in the device is turbulent, so the effect of sand particle viscosity is small. The Basset force is significant only in the early acceleration, and the Magnus force is only considered when the particles rotational motion is very strong, so both of them can be ignored. In summary, in the actual numerical simulation, in order to accelerate the convergence and reduce the calculation of numerical calculation, the interphase force is only considered resistance.

3.1. Inlet boundary conditions

The inlet flow velocity is based on the inlet, which is perpendicular to the inlet plane, and its dimensions are determined by the inlet volume and the inlet area. The turbulence intensity at the inlet boundary is calculated as follows[9]:

$$I = 0.16\,\mathrm{Re}_{\mathrm{DH}}{}^{-0.125} \tag{6}$$

The inlet velocity is 7.2 m/s, the output is free-flow, the overflow boundary is characterized by escape, the bottom flow is trap, and the wall is a no-slip boundary; the method is solved in the form of a standard wall function. The density of the incident sand particles is 2600 kg/m^3, the volume concentration of sand is 1%, and the particle size of the incident sand particles is Rosin-Rammler distribution, with a minimum diameter of 1×10-5m, a maximum diameter of 2×10-4m, and an average diameter of 1×10-4m.

3.2. Outlet boundary conditions

An optional free-drainage outlet is provided between the overflow outlet and the underflow outlet boundary. In the solution of the DPM model, the boundary characteristics of the overflow are denoted by escape, while the bottom boundary is denoted by trap.

3.3. Wall boundary conditions

The wall with no slip boundary is used and the standard wall function is used to calculate it. The flow field and performance are investigated and the velocity and pressure distributions are shown in Fig. 3 and Fig. 4, respectively.

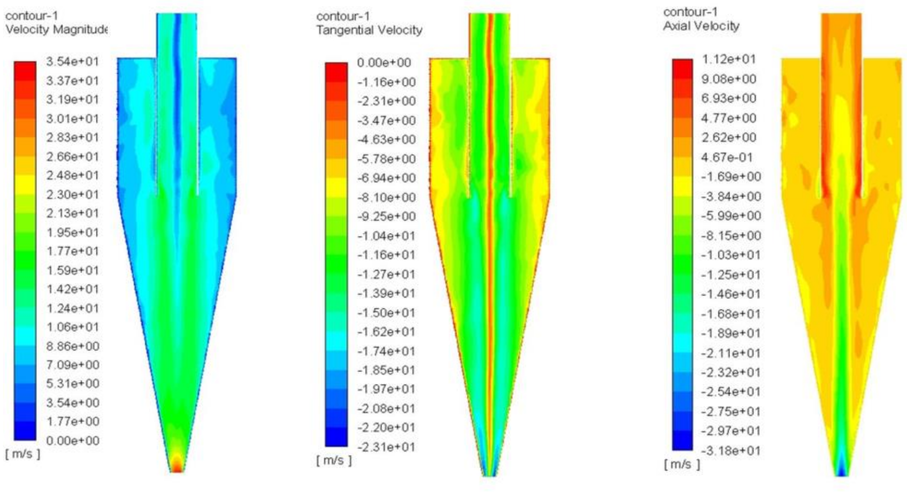

(a) Combined velocity; (b) Tangential velocity; (c) Axial velocity

Fig. 3 Velocity distribution cloud diagram of the cyclone

From Fig. 3(a), it can be seen that the peak value of the combined velocity appears near the bottom flow opening, which indicates that the separated sand particles can be quickly excluded from the cyclone. The lower velocity is generated at the center of the cyclone axis and the wall, and the velocity distribution is roughly "M" type. The negative tangential velocities in Fig. 3(b) indicate the opposite direction of the coordinate values. From the figure, it can be seen that, similar to the combined velocity, the tangential velocity at the wall and the center of the shaft is smaller, and the distribution is also called "M" type. The conical section of the two phases of water and sand is the main area of separation, in which the two phases are separated due to the large centrifugal acceleration produced by the density difference. In Fig. 3(c), the negative axial velocity in the graph indicates the opposite direction to the coordinate value, which is negative on behalf of the direction of the flow to the bottom flow opening and positive on behalf of the direction of the flow to the overflow opening. From the figure, it can be seen that the maximum flow velocity in the overflow port is 11.2 m/s and the maximum flow velocity in the underflow port is 31.8 m/s, which indicates that the separated oil and water phases can be excluded from the separator faster, avoiding back-mixing in the cyclone and thus affecting the separation efficiency.

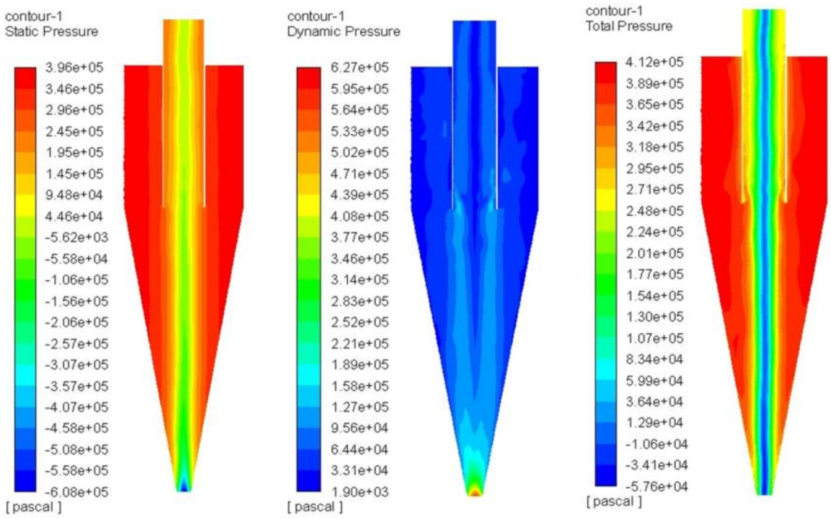

(a) static pressure; (b) dynamic pressure; (c) total pressure

Fig. 4 Cloud diagram of pressure distribution in cyclone

From Fig. 4(a), it can be seen that the static pressure from the wall to the axis gradually decreases along the radial direction and negative pressure appears near the axis, the distribution of static pressure is axial and symmetric. The fluid flowing into the separation device from the tangential inlet undergoes rotation and the rotating fluid generates centrifugal force in a radial outward direction. In order for the centrifugal force to be balanced in a radial direction, the fluid has to develop a pressure difference inside, and therefore the static pressure decreases radially from the outside to the inside. Fig. 4 (b) can be seen, the dynamic pressure in the center of the cyclone axis and the wall of the lower, the dynamic pressure distribution is roughly "M" type, similar to the combined velocity and tangential velocity. This is due to the fluid dynamic pressure for the fluid has the size of the specific kinetic energy, so the distribution of dynamic pressure mainly depends on the distribution of the total velocity. The maximum dynamic pressure occurs near the bottom flow opening, which is about 0.6 MPa. From Fig. 4(c), it can be seen that along the radial direction from the wall to the shaft, it shows a distribution pattern of slow decay and then rapid decay. Due to the viscous vortex motion of the liquid, the rotation of the cyclone wall flow is not ideal, and can only be regarded as a kind of approximate "free vortex", and in the radial interface, due to the energy loss is less, so it can make the overall pressure on the wall of the free area of the vortex gradually weakened to the interior. Under the condition that the incident sand particle size is Rosin-Rammler distribution, the minimum diameter is 1×10-5m, the maximum diameter is 2×10-4m, and the average diameter is 1×10-4m, the desander desanding efficiency of 91.3% is obtained through numerical simulation, the average diameter of the sand particles in the water outlet is 68.54 μm, the mass flow rate of the sand phase is about 2.86 kg/s, and the average velocity of the water outlet is 9.3 m/s. The sand phase has a mass flow rate of about 2.86 kg/s, and the water outlet has an average velocity of 9.3 m/s. The water outlet has an average velocity of about 1.3 m/s. The average flow rate was 9.3 m/s.

In addition, it should be explored to discuss the separation efficiency situation of the cyclone in the case of different particle sizes, i.e., classification efficiency, the particle efficiency of the cyclone under different single particle sizes was investigated, and the results are shown in Fig. 5.

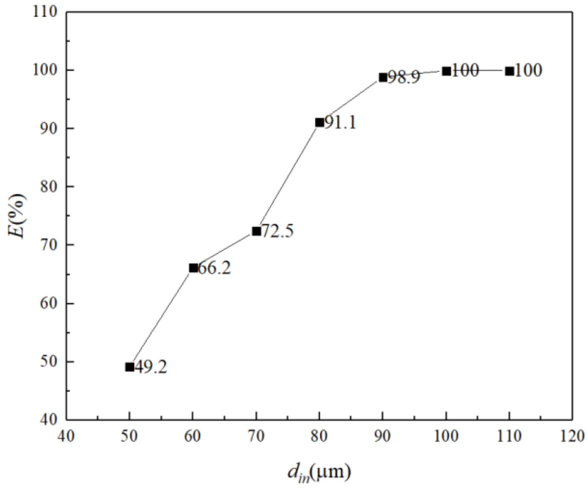

Fig. 5 Grain level efficiency of cyclone

As can be seen from Fig. 5, with the increase of the inlet sand grain diameter, the separation efficiency of the cyclone first increases rapidly, and then increases very slowly. When the inlet diameter is 80 μm, the separation efficiency of the cyclone has reached 91.1%; when the inlet diameter reaches 100 μm or more, the cyclone can completely separate the sand particles, and the separation efficiency reaches 100%.

4. NUMERICAL SIMULATION STUDY OF COARSE-EFFECT FILTER AND FINE-EFFECT FILTER

Coarse-effect filter and fine-effect filter geometry is identical, are based on metal wire mesh filter element, only the pore size of the filter element is different, embodied in the numerical simulation needs to be adjusted to the relevant parameter settings of the porous media[10]. Based on the numerical simulation software, combined with the porous media filtration theory, a three-dimensional model of the filter is established to analyze the flow characteristics within the wire mesh filter.

The fluid model of the wire mesh filter is meshed with a full tetrahedron with a mesh quality of 0.35 or more, and the delineation of the mesh is shown in Fig. 6. The mesh-independence test is performed to verify the feasibility of the computational method and the correctness of the results, and this step is essential. Therefore, the overall mesh is encrypted and the grid numbers are 1120000, 3570000 and 7450000, and the calculation is performed under the same operating conditions. After calculation, the inlet pressure values are 114467.2 Pa and 114693.2 Pa. The difference between them and the above inlet pressure value of 113907.4 Pa is 559.8 Pa and 785.8 Pa, i.e., 4.45% and 6.25%, respectively. It can be concluded that when the number of grids is 3570000, we find that continuing to increase the number of grids has less impact on the calculation results. So, 3570000 grid is proposed for the numerical visualization of the filtration equipment.

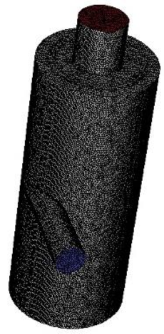

Fig. 6 Wire mesh filter grid

Based on the physical properties of the wire mesh ground, the modeling assumptions are as follows [11]:

(1) Only consider the state after it has been stabilized, not counting the initial and terminal moment, then the whole process is a constant flow (constant flow);

(2) The flow process does not take into account the effect of temperature, then it is not considering the heat transfer process of the metal mesh wire, then the whole process is isentropic flow;

(3) Neglect the effect of deformation of the filter at low temperatures. Since the flow is a constant process, the energy equation of the fluid is not considered.

The inlet condition adopts the velocity inlet, the inlet velocity is the desander water outlet velocity 9.3 m/s, the outlet is the pressure outlet, the pressure is 1 atmosphere, the average pressure at the inlet can be regarded as the cartridge pressure drop value, and the wall adopts the no-slip boundary. The density of the incident sand particles is 2600 kg/m^3, the mass flow rate of the sand body is 2.86 kg/s, and the average particle size of the incident sand particles is 6.9×10-5m.

The inlet flow rate versus pressure drop relationship was obtained based on the wire mesh cartridge test, and the pressure drop-velocity curve was fitted:

$$\Delta p = Av^2 + Bv \tag{7}$$

Compare this curve equation with the source term equation for porous media:

$$Si = -\left(\frac{\mu}{\alpha}v + \frac{C_2}{2}\rho|v|v_i\right) \tag{8}$$

The viscosity coefficient $\frac{1}{\alpha}$ and inertia coefficient C_2 of the porous medium can be obtained.

After conversion, the viscous coefficient and inertia coefficient of the wire mesh with a pore size of 100 μm can be obtained: $\frac{1}{\alpha}$ = 3.21028×10-9, C_2 = 8.18×102m2.

The coefficient of viscosity and number inertia of the wire mesh with a pore size of 5 μm : $\frac{1}{\alpha}$ =6.25463×10-10, C_2 =5.34×104m2.

The velocity and pressure fields inside the roughing filter were investigated for a 600 mm cartridge length. Fig. 7(a) shows the velocity cloud of the coarse-effect filtration equipment. From the figure, it can be seen that due to the sudden change of filter area, the flow velocity is low in the area of the filter cartridge, while the velocity increases after flowing through the filter element, especially at the exit position of the filter. The flow velocity distribution on the surface of the filter element is more uniform. The flow velocity is highest near the inlet. After the filter cartridge, the flow velocity is lower and irregular velocity fluctuations occur, with higher flow velocity in the middle of the cartridge, i.e., near the inlet height, and lower flow velocity at the bottom wall of the device. Fig. 7(b) shows the velocity vector diagram of the coarse-effect filtration equipment. As can be seen from the figure, similar to the velocity cloud diagram, the flow velocity in the area after the filter core is low, and the direction of the flow velocity is more chaotic, and the direction of the flow velocity near the inlet height has a large offset, indicating that the turbulence in the flow field after the filter core is more intense. After the fluid enters the filter, it rotates along the tangential direction, and part of the fluid enters the center region of the filter through the filter core, and then changes the flow direction to flow out from the top outlet. Fig. 7(c) shows the static pressure cloud diagram of the coarse-effect filtration equipment. As can be seen from the figure, before flowing into the filter element, the pressure value is higher and more evenly distributed. Due to the resistance of the cartridge, the pressure decreases suddenly and continuously along the flow direction. At the inlet of the cartridge, the change of static pressure due to the change of air flow direction causes a change of static pressure, and the pressure at the outlet is slightly rebounded. Pressure changes inside the cartridge are minimal, with sudden changes concentrated in the cartridge passages and at the outlet of the unit.

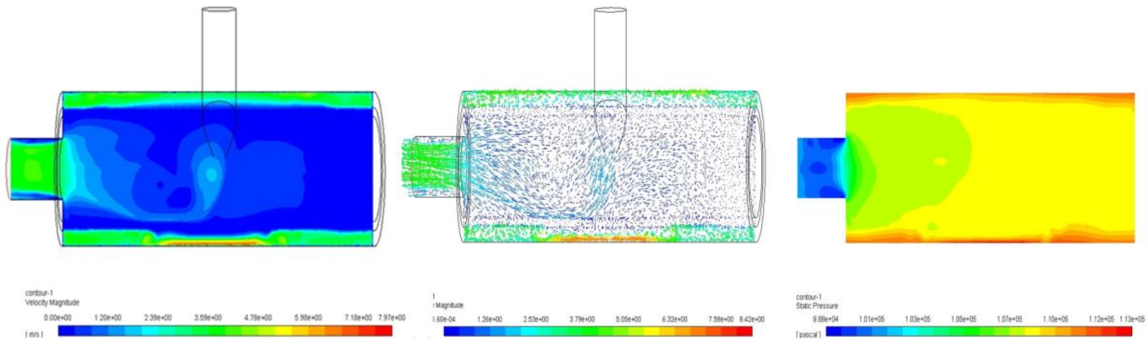

(a) Velocity cloud diagram (b) Vector cloud diagram (c) Static pressure cloud diagram

Fig. 7 Cloud diagram of coarse-effect filtration equipment

5. CONCLUSION

Under the condition that the density of incident sand particles is 2600 kg/m^3, the mass flow rate of sand body is 2.86 kg/s, and the average particle size of incident sand particles is 6.9×10-5m, the desanding efficiency of the roughing filter is obtained by numerical simulation to be about 83.4%, the average diameter of exported sand particles is 32.18 μm, the mass flow rate of the sand phase is about 0.94 kg/s, and the average velocity of exported flow rate is 5.2 m/s. Using these parameters as the inlet conditions of the fine filter, the final sand removal rate obtained is 100%, which means that under the simulated conditions, the sand particles at the inlet can be completely removed by the three-stage treatment process of desander-coarse filter-fine filter. Of course, the numerical simulation method contains various assumptions and approximations, and there are still some differences with the actual situation, but the combination of indoor experiments and numerical simulation methods have verified the high-efficiency filtration performance of the three-stage filtration process.

REFERENCES

[1] Cui Yuanyuan. Applied research on geothermal tail water recharge test in Shandong province[J]. Shandong Land Resources,2019;35(7):64-71.

[2] CAO Qian,FANG Chaohe,LI Yun,et al. Development status and revelation of geothermal recharge at home and abroad[J]. Oil Drilling Process,2021,43(02):203-211.

[3] XU Wei, PAN Xiaoping, YANG Yajun, et al. Current status of geothermal recharge research in Beijing[J]. Geothermal Energy. 2012;(3):11-13.

[4] WANG Haigang,LIU Shi. Application and comparison of different turbulence models in three-dimensional numerical simulation of cyclone separators[J]. Thermal Power Engineering,2003;18(4):337-342.

[5] Gao Xinzhi. Evaluation modeling of recharge capacity of thermal storage in porous sandstone in Tianjin [D]. China University of Geosciences (Beijing), 2018.

[6] Qi Jagang. Hydrocyclone classification performance analysis and its improvement [D]. Harbin Institute of Technology, 2021.

[7] Wang Xuepeng, Liu Huan, Jiang Shujie, et al. Experimental study of sandstone thermal storage recharge in sedimentary basins--A case study of Yucheng City, Shandong Province[J]. Geological Review, 2020, 66(2):8.

[8] YUAN Linzhu, ZHU Liping, GENG Fan et al. Gas-solid two-phase flow and numerical simulation[M]. Southeast University Press,2012.

[9] JI Feng. Development of high pressure cyclone desanding device[J]. Piping Technology and Equipment,2022(01):44-46+51.

[10] LI Bingping, YE Chengming, HE Jibin, et al. Fracturing and injection test of recharge source in Shandong Wenshitang geothermal field[J]. Prospecting Engineering(Geotechnical Drilling Engineering),2014;41(12):6-10.

[11] HAN Shuai. Field test of hydrocyclone separation technology for treatment of thick oil produced water[J]. Oil and gas field surface engineering,2020,39(09):44-47.